




Exploring crystal structure by three-dimensional atomic density distribution from molecular dynamics simulations

Cheng-Rong Hsing ^{1,*}, Duc-Long Nguyen ¹ and Ching-Ming Wei ^{1,2,†}

¹*Institute of Atomic and Molecular Sciences, Academia Sinica, Taipei 10617, Taiwan*

²*Institute of Physics, Academia Sinica, Nankang 11529, Taiwan*



(Received 17 March 2022; revised 15 July 2022; accepted 19 July 2022; published 10 August 2022)

Predicting crystal structure has been one of the core issues in materials research. X-ray diffraction data can generally be used to fit and refine the positions of atoms within the unit cell. However, for a system with part of its atoms diffusing or hopping below the melting temperature, the atoms inside the crystal begin to vibrate, diffuse, or hop when its temperature gradually rises. Even using the partial-occupancy concept, it becomes difficult or impossible to fit the structure due to the trial-and-error characteristic of refinement. More importantly, the limited partial-occupancy positions are insufficient and inappropriate to describe material systems containing diffusing or hopping atoms. To address this shortcoming, we proposed to perform molecular dynamics simulations and then add up all the positions of diffusing atoms in each time step to form a three-dimensional atomic density distribution into the primitive or conventional unit cell. The maximum atomic density points correspond to the partial-occupancy positions in x-ray diffraction data. The connected atomic density distribution identifies and defines the diffusing paths for mobile atoms within the crystal.

DOI: [10.1103/PhysRevMaterials.6.083601](https://doi.org/10.1103/PhysRevMaterials.6.083601)

I. INTRODUCTION

X-ray diffraction (XRD) is one of the most powerful experimental methods for studying crystal structures. The experimental spectra of XRD can be easily inverted to obtain the crystal structure for a simple material system with a fixed and known composition. However, because of the increasing independent dimensionalities of the crystal structure in complicated material systems, XRD results may become difficult or even impossible to invert to obtain complete, correct atomic structures. Furthermore, for a system in which atoms begin to diffuse or hop inside the crystal as temperature increases, it becomes difficult to fit the structure using XRD data without the concept of partial occupancy [see Figs. 1(a)–1(d) below]. Even with partial occupancy, the obtained crystal structures may not be correct and are unreliable for some systems. The liquidlike thermoelectric (TE) material is one example; its crystal structure is solid, but some of its atoms behave like liquids. Typically, atoms diffuse through the crystalline sublattice (solid framework), resulting in an intrinsically low lattice thermal conductivity [1–5]. Because of the highly mobile atoms in the liquidlike TE materials, atomic occupation probabilities at various Wyckoff sites refined from XRD data are naturally partially occupied [6–9] and difficult to fit or determine. Using Ag_8GeTe_6 as an example, four different partial-occupancy results of Ag atoms were reported in the literature as shown in Figs. 1(a)–1(d). One can see that the fitted positions of Ge and Te atoms are nearly identical, but the fitted positions of Ag atoms are quite different. One cannot

judge which result is correct or reliable, and we require a method to resolve this kind of partial-occupancy difficulty.

This study proposes using *ab initio* molecular dynamics simulations (MDSs) to overcome the deficiency of the partial-occupancy concept used in XRD. It is important to minimize the statistical error when performing MDSs, as discussed by He *et al.* [10]. They concluded that simulation at high temperature and with a system with diffusivity ranging from 10^{-7} to 10^{-5} cm^2/s is suitable for the MDSs to have enough diffusion and jumping processes to obtain more accurate diffusional properties. The diffusivity of a system containing liquidlike mobile atoms is usually within this range [11–18]. Xie *et al.* [11] used *in situ* scanning transmission electron microscopy and MDSs to study the diffusion dynamics of Ag atoms in superionic AgCrSe_2 . Molecular dynamics (MD) trajectories were used to calculate probability distribution and the time-dependent Van Hove correlation functions. Xie *et al.* found that Ag diffusion is slow compared with the vibrations and concluded that the crystal disorder is the main reason for the ultralow thermal conductivity. de Klerk *et al.* [12] used MDSs to obtain Li-ion density and its jump processes to study the Li-ion conductivity in argyrodite solid electrolytes. They found that the Li-ion conductivity could be improved by optimizing the halogen distribution. Without any phase change, $\beta\text{-Cu}_2\text{Se}$ exhibits abnormal temperature-dependent thermal properties. Kim *et al.* [13] performed molecular dynamics calculations and found that the bond length of Cu-Cu and Cu-Se decreases with increasing temperature. At $T \approx 800$ K, Cu presents an apparent thermal disorder structure, which they also confirmed through experimental studies. Zhuo *et al.* [14] and Wang *et al.* [15] also used MDSs to study the diffusion mechanism of the high-temperature phase of Cu_2S and Cu_2Se and hexagonal Cu_2S , respectively. They used MDS

*crhsing@gate.sinica.edu.tw

†cmw@phys.sinica.edu.tw

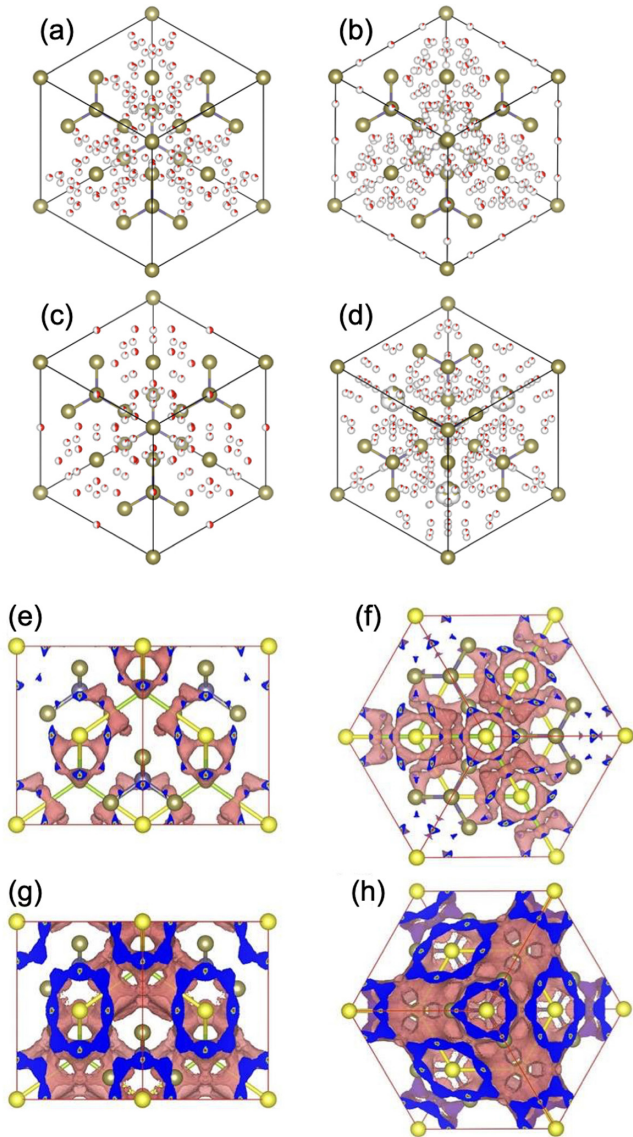


FIG. 1. (a)–(d) XRD fitted crystal structures of Ag_8GeTe_6 reported in Refs. [20–22]. The red-white spheres represent the partially occupied Ag sites. Corresponding crystal structures were obtained from the Crystallography Open Database (COD) [23,24] (Table S2 of the Supplemental Material). (e) and (f) 2D constant-density surface, with density equal to $1.5 \times 10^{-2} a_0^{-3}$, of the Ag 3D atomic density distribution for Ag_8GeTe_6 at 300 K viewed along the [110] and [111] directions, respectively. (g) and (h) Same as (e) and (f), but for a 2D constant-density surface with density equal to $4.0 \times 10^{-3} a_0^{-3}$. The maximum Ag density is $4.95 \times 10^{-2} a_0^{-3}$.

trajectories to investigate the liquidlike Cu diffusion property and characterize the structural properties with radial distribution functions. The Cu diffusivity coefficients are around 10^{-6} – 10^{-5} cm^2/s , exhibiting a liquidlike behavior. In their work on Cu_2X , Kumar *et al.* [17] discussed in detail the range of temperatures using MDSs, including the diffusion coefficient and the energy barrier. Through the analysis of MDS results based on a 30-ps trajectory length, they found that the activation energy barrier of Cu atoms was consistent with the reported experimental values and observed

the liquidlike diffusion of Cu ions at higher temperatures. In addition, Wych *et al.* [18] have performed MDSs using two force fields to study the dynamics of crystalline protein. They simulated x-ray diffraction with 400-ns MD trajectories to show that crystalline proteins exhibit liquidlike motions. In general, MDSs are performed to study mobile atoms' diffusion behavior; most analyses focus on the pair distribution function, mean-square displacements, velocity autocorrelation functions, or atomic trajectory. Nevertheless, no systematic molecular dynamics study combined with the concept of partial occupancy exists in crystals. As one might imagine, what has been measured in XRD or single-crystal x-ray diffraction (ScXRD) is a time average of the material system. Therefore the averaged structure of an MDS over a time domain should be helpful and a good hint or starting point for XRD or ScXRD fitting. By averaging enough time frames of atomic structures from MDS results, a three-dimensional atomic density distribution function (3D-ADDF) of the studied material system can be easily obtained. This 3D-ADDF will automatically reveal accurate partial-occupancy positions by maximum atomic densities without random guessing, thereby overcoming the difficulty and limitation of the partial-occupancy concept in XRD.

To begin MDSs for complicated systems with unclear ground-state structures, we use the random structure search with object (RSSWO) scheme [19]. This method can generate the initial configurations randomly and find the correct lowest energy structures if the number of initial configurations is large enough. Systems with varying initial configurations are relaxed until local minimum energy structures obtain, and a few lowest energy structures are used for MDSs. In this paper, molecular dynamics simulations were run on various phases of Ag_8GeTe_6 , Ag_8SiTe_6 , Cu_2S , and Cu_2Se to obtain an atomic density distribution function that contains the most basic and essential structural information in detail. Because the trial-and-error characteristic of XRD analysis is technically demanding and time-consuming, it is not guaranteed that a clear answer will be obtained for complicated material systems. This work aims to demonstrate how to use MDSs to obtain information about the 3D atomic density distribution in the primitive or conventional unit cell by averaging the MDS trajectory frames. This 3D-ADDF will automatically reveal the crystal symmetry, the partial-occupancy positions, and the mobile atoms' diffusing or hopping pathways and regions. The accuracy of the 3D-ADDF, which has provided the positions and occupancy of various types of atoms, can then be double-checked by comparing it with an experimentally fitted XRD structure. In reality, the 3D-ADDF can be considered as an extension of the continuous model for the partial occupancy used in XRD.

The rest of this paper is structured as follows. Computational details are provided in Sec. II. We present and discuss the MDS results for the Ag_8GeTe_6 , Ag_8SiTe_6 , Cu_2S , and Cu_2Se systems in Sec. III. The obtained 3D atomic density distribution function will be used to demonstrate that the partial occupancy concept used in x-ray diffraction data has limitations in all of the systems studied here. As a result, it is preferable and inevitable to define and employ the 3D-ADDF as a continuous extension model for the partial-occupancy

concept used in XRD. Section IV summarizes and presents our conclusions.

II. COMPUTATIONAL METHOD

The first-principles molecular dynamics calculations were performed based on the density functional theory (DFT) [25,26] using the plane-wave-based Vienna *ab initio* simulation package [27,28] with the projector augmented-wave (PAW) potentials [29]. For all systems studied, the exchange-correlation functional is treated by the generalized gradient approximation with the Perdew-Burke-Ernzerhof form [30], and the plane-wave cutoff energy is set to 300 eV. We carried out the random structure searching with object [19] calculations to generate initial crystal structures and then performed DFT calculations to obtain the lowest energy optimized structures. In order to explore the structural configuration space more completely, we took at least five lowest energy structures obtained from RSSWO and DFT optimizations as the starting points to perform MDSs. The Γ k point was used for all the MDSs and was performed using the *NVT* ensemble scheme. The trajectory time frames from all different MDS runs at a constant temperature were then combined, averaged, and normalized into the unit cell to yield a 3D atomic density distribution in units of atoms per a_0^3 ($a_0 = 0.529$ Å, the Bohr radius). Moreover, the 3D atomic density distribution was applied with symmetry operations hinted at by the 3D-ADDF. In practice, after a long MD run, we added all atoms' positions at each time step into the primitive or conventional unit cell divided by $100 \times 100 \times 100$ grid points to obtain the temperature-dependent atomic density functions. We then utilized the Visualization for Atomic and Structural Analysis (VESTA) program [31] to view, analyze, and plot the isosurfaces of 3D atomic density distribution functions.

III. RESULTS AND DISCUSSION

This section presents the results of molecular dynamic simulations for two types of systems: (i) Ag-based argyrodites Ag_8GeTe_6 and Ag_8SiTe_6 and (ii) Cu_2X -based materials Cu_2S and Cu_2Se . We will discuss the structure of the 3D atomic density distribution function in detail to understand its implications and how it relates to the partial-occupancy concept used in x-ray diffraction. Because the 3D-ADDF is derived from MDSs, it is expected to be temperature dependent, and we will demonstrate the effect using Ag_8SiTe_6 . It is also possible to obtain the value of partial occupancy directly in cases where the 3D-ADDF has isolated local maxima; we will present the results of the Cu_2S hcp phase as an example.

A. Ag-based argyrodites: Ag_8GeTe_6 and Ag_8SiTe_6

The Ag-based argyrodite-type compounds Ag_8GeTe_6 and Ag_8SiTe_6 , with *p*-type semiconductor characteristics, have the same crystal structure [20,32]. The structure suggested by experiment is shown in Fig. 2, representing a cubic unit cell with a $F\bar{4}3m$ space group symmetry. Previous studies reported that Ag atoms have a high degree of freedom, and their liquidlike nature would effectively scatter phonons, resulting in a very low lattice thermal conductivity [2]. For Si (Ge) and Te atoms, it has been reported to form the SiTe_4 (GeTe_4)

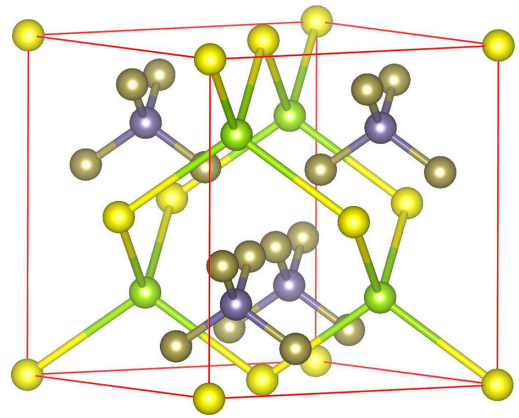


FIG. 2. Structural model of Ag_8SiTe_6 suggested by experiment with a $F\bar{4}3m$ symmetry (space group 216). Yellow balls indicate the Te atoms at 4a sites, and green balls indicate the Te atoms at 4c sites. Dark yellow Te atoms (at 16e sites) and purple Si atoms (at 4d sites) form a tetrahedral framework. Here, we only present the positions of Si and Te atoms because the positions of Ag atoms are not well determined.

tetrahedral framework [20,32]. We take Ag_8SiTe_6 (see Fig. 2) as an example to illustrate its detailed crystal structure. The Te atoms are found at three different locations in space group 216 ($F\bar{4}3m$) and can be divided into two groups. The tetrahedral framework is composed of dark yellow Te (at 16e sites) and purple Si atoms (at 4d sites). Yellow Te (at 4a sites) and green Te (at 4c sites) are loosely bonded to silver atoms and have larger atomic displacements than Te at 16e sites [32]. The thermal fluctuation of the yellow Te (4a) and green Te (4c) sites is related to the large distribution observed at neighboring silver sites [21,22]. Thus the entire structure can be reformulated as $\text{Ag}_8(\text{SiTe}_4)\text{Te}_2$.

To investigate the probable temperature influence on the behavior of Ag atoms induced by the diffusion and hopping process, we performed MDSs at various temperatures. We initially modeled the Ag_8GeTe_6 (or Ag_8SiTe_6) crystal structures with Ge (or Si) and Te atoms fixed at their $F\bar{4}3m$ symmetry sites; then we utilized the RSSWO method to generate 300 initial Ag atomic configurations and used DFT to perform structural optimization. We then took five to ten of the lowest energy structures and performed MDSs at a temperature of 300 K for Ag_8GeTe_6 and 300 K and 687 K for Ag_8SiTe_6 . We used Ag_8SiTe_6 as an example. The optimized results for the 50 lower energy structures at 0 K are shown in Fig. S1 of the Supplemental Material [33]. RSSWO results show a nearly continuous increase in the system's total energies and indicate a rich configuration space for systems containing liquidlike mobile atoms. The first six lowest energy structure configurations used for MDSs span an energy range of 0.319 eV (or 5.3 meV/atom; see Table S1 of the Supplemental Material). This small span of the energy range ensures that the effect of initial structure configurations will be washed out by MDSs.

The molecular dynamics simulations for Ag_8GeTe_6 were run for 200 ps, with 2-fs time steps and with the *NVT* ensemble. Figures 1(e) and 1(f) show a 2D constant-density surface of the Ag 3D atomic density distribution averaged from five MDS runs seen along the [110] and [111] directions

for Ag_8GeTe_6 at 300 K. It is fascinating to notice that the Ag density accumulates around the circles on the planes that cut through the middle of the line connecting yellow Te (4a) and green Te (4c) atoms (also refer to Fig. 2). Another intriguing aspect is that there are 16 connecting lines of yellow Te (4a) and green Te (4c) pairs and 32 Ag atoms inside each unit cell, therefore implying that two Ag atoms are associated with one connecting line of yellow and green Te atoms. Furthermore, one can certainly look at a constant lower density surface, for example, $4.0 \times 10^{-3} a_0^{-3}$, of the 3D-ADDF as shown in Figs. 1(g) and 1(h). It is easy to see that the distinct Ag high-density surfaces are now connected through the whole unit cell. These interconnected distribution surfaces vividly show and characterize the Ag diffusing pathways and regions within the crystal.

The MDSs for Ag_8SiTe_6 at 300 and 687 K were run for 400 ps with 2-fs time steps and with the NVT ensemble. At 687 K, as shown in Fig. S2 of the Supplemental Material, MDSs initiated from any of the six configurations indeed show a distribution of the liquidlike atoms similar to those obtained from the other, different initial configurations. The behavior of mobile atoms in liquidlike systems here differs from that of solid systems such as the Mott insulator oxides [34,35], iron selenide [36], or halide perovskites [37]. For those systems, a variety of similar configurations with large unit cells have lower energies than the commonly accepted small unit cell deduced from XRD. As the temperature rises, the vibration and diffusion of mobile atoms increase, and the trajectories of mobile atoms show a much more dispersed diffusion nature. With a long-time average, the results from different initial structures tend to show a similar distribution. As expected, longer MD runs are needed to achieve the spread-out diffusion nature at medium temperature. Alternatively, at the lower temperatures where the mobile atoms are unlikely to hop or diffuse, spatial averaging procedures to add up more MD runs from different initial structures can also obtain the global averaged atom density distribution. The MD trajectories of the ten lowest energy configurations of Ag_8SiTe_6 at 300 K (right panels in Fig. S3 of the Supplemental Material) show the slow diffusivity of Ag as compared with its diffusion behavior at 687 K. When we sum up the total trajectories of the Ag atoms for ten different structures, the overall summed atom distribution of Ag trajectories agrees well with that at 687 K, as evident from the bottom right panel in Fig. S3 of the Supplemental Material.

Figures S4 and S5 of the Supplemental Material show the mean-square displacement and pair correlation function for the studied Ag-based argyrodite and Cu_2X systems, respectively. For the mean-square displacement calculations, instead of sampling the whole trajectory, we tested different average time intervals (~ 10 –60 ps) to get a well-averaged result. From the results of Ag_8SiTe_6 at 687 K and Cu_2S and Cu_2Se in the high-temperature fcc phase, the mean-square displacement curves have almost the same slopes as the average time fractions increase, which indicates that MDSs have a short convergent time at high temperature. However, the mean-square displacement results at medium temperatures show the slowdown of the dynamics, and the minimum convergent time would be longer, especially for Ag_8GeTe_6 and Ag_8SiTe_6 at 300 K. The pair correlation function for Ag-Ag pairs also

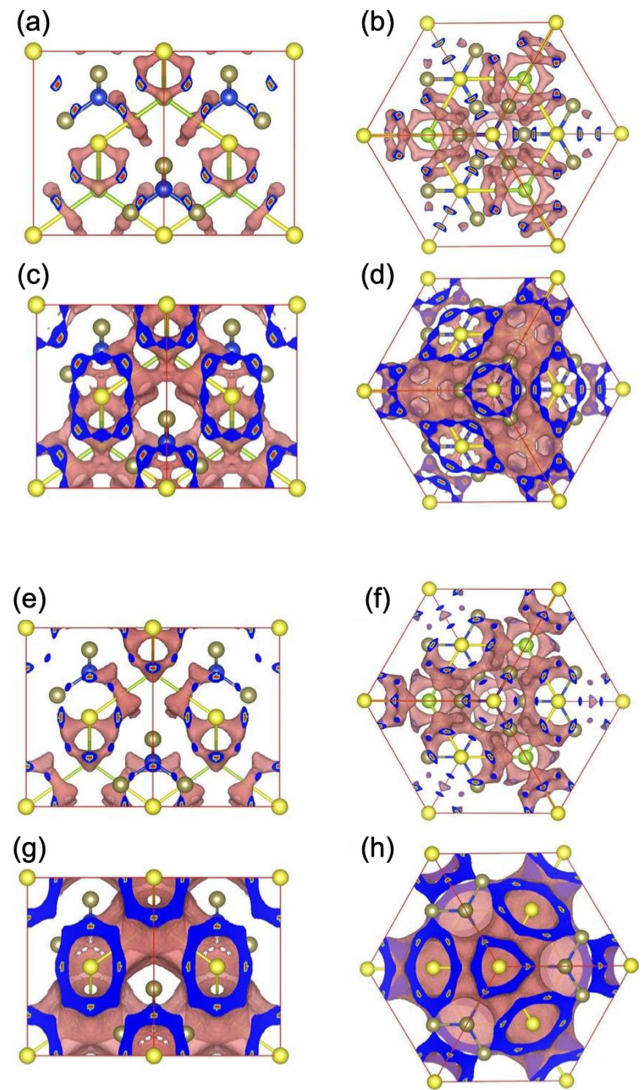


FIG. 3. 3D atomic density distribution of Ag_8SiTe_6 at different temperatures. (a) and (b) 2D constant-density surface, with density equal to $2.0 \times 10^{-2} a_0^{-3}$, of the Ag 3D atomic density distribution at 300 K viewed along the [110] and [111] directions, respectively. (c) and (d) Same as (a) and (b), but for a 2D constant-density surface with density equal to $4.5 \times 10^{-3} a_0^{-3}$. The maximum Ag density is $8.89 \times 10^{-2} a_0^{-3}$. (e) and (f) 2D constant-density surface, with density equal to $1.15 \times 10^{-2} a_0^{-3}$, of the Ag 3D atomic density distribution at 687 K viewed along the [110] and [111] directions, respectively. (g) and (h) Same as (e) and (f), but for a 2D constant-density surface with density equal to $3.5 \times 10^{-3} a_0^{-3}$. The maximum Ag density is $3.45 \times 10^{-2} a_0^{-3}$.

shows a dependence on the initial configurations for the MDS run at 300 K; see the results for Ag_8SiTe_6 shown in the top left panel in Fig. S5 of the Supplemental Material.

Figures 3(a)–3(d) depict the 2D constant-density surface of the Ag 3D atomic density distribution function at 300 K when viewed along the [110] and [111] directions at medium ($2.0 \times 10^{-2} a_0^{-3}$) and low ($4.5 \times 10^{-3} a_0^{-3}$) density values; Figs. 3(e)–3(h) show similar plots at 687 K at medium ($1.15 \times 10^{-2} a_0^{-3}$) and low ($3.5 \times 10^{-3} a_0^{-3}$) density values. The findings are comparable to those of Ag_8GeTe_6 at both

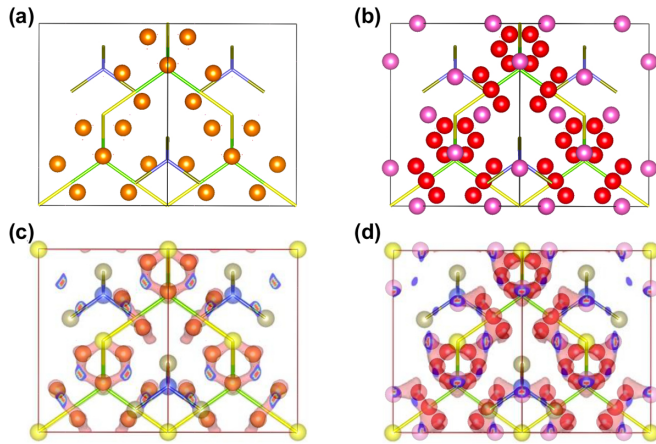


FIG. 4. (a) and (b) The three partially occupied Ag positions at Ag(1), Ag(2), and Ag(3) sites proposed by Boucher *et al.* [32] viewed along the [110] direction. Orange balls in (a) indicate the Ag(1) positions at the $48h$ Wyckoff sites. Pink and red balls in (b) indicate the Ag(2) and Ag(3) positions at the $48h$ and $96i$ Wyckoff sites, respectively. (c) Combination of (a) and Fig. 3(a). (d) Combination of (b) and Fig. 3(e).

temperatures. When the Ag density value is reduced from high or medium to low, the isolated Ag high-density regions are connected and pass through the different unit cells. These connected distribution surfaces define the diffusing routes and regions for Ag atoms inside the crystal. After a thorough examination, it is discovered that the 2D constant-density surfaces at 687 K are flatter than those at 300 K, as evidenced by the maximum Ag density at 300 K ($8.89 \times 10^{-2} a_0^{-3}$) being much greater than that at 687 K ($3.45 \times 10^{-2} a_0^{-3}$). Clearly, the spreading nature of Ag atoms in the 3D-ADDF of Ag_8GeTe_6 and Ag_8SiTe_6 explains why fitting the Ag partial occupancy of XRD is so difficult and perplexing [see Figs. 1(a)–1(d)]. Thus it is preferable to characterize and comprehend systems using the 3D atomic density distribution function rather than the partial occupancy employed in XRD.

In addition, based on the XRD measurements of Ag_8SiTe_6 at room temperature, Boucher *et al.* [32] found that the silver atoms could partially occupy three sites: the orange Ag(1), pink Ag(2), and red Ag(3) balls as shown in Figs. 4(a) and 4(b). The results indicate Ag(1) and Ag(2) at $48h$ sites with 16.82 and 25.6% occupation probability, respectively, and Ag(3) at $96i$ sites with 12.2% occupation probability. Their x-ray analysis revealed that Ag atoms at the Ag(2) and Ag(3) sites had a larger atomic motion. Figures 4(c) and 4(d) depict the combination of the 2D constant-density surface of Fig. 3(a) with Fig. 4(a) and of Fig. 3(e) with Fig. 4(b). In comparison to the silver atom locations provided in Ref. [32], the 3D atomic density distribution of Ag_8SiTe_6 at 300 K agrees well with the result suggested by experiment, where Ag(1) sites are located at the circular rings of Ag densities. Furthermore, the Ag(2) and Ag(3) sites suggested by experiment agree fairly well with the 3D atomic density distribution of Ag_8SiTe_6 at 687 K. As the temperature rises, the vibration and diffusion of Ag atoms increase, and the 3D-ADDF of Ag_8SiTe_6 at 687 K [see Figs. 3(e)–3(h)] shows a more spread-out nature than at 300 K [see Figs. 3(a)–3(d)];

this might explain why Ag atoms vibrate and fluctuate so much at Ag(2) and Ag(3) sites at high temperatures. It is fascinating to learn that the structural model by Boucher *et al.* [32] captures the most of maximum-Ag-density regions in the 3D-ADDF of Ag_8SiTe_6 , but the experimental findings do not reveal the diffusion pathways and regions obtained by the 3D-ADDF. It is certainly interesting to see the results of the framework atoms. For example, the experimental spectra of XRD can be easily inverted to obtain the positions for Te atoms situated at some symmetry positions. The 3D atomic density distribution obtained from MDSs agrees well with the Te atoms' positions suggested by experiment (see Fig. S6 of the Supplemental Material), demonstrating the accuracy and reliability of the 3D-ADDF.

B. Cu_2S and Cu_2Se

Cu_2S has been reported to exist in three phases: the low-temperature monoclinic phase (low chalcocite, temperatures below 380 K), the hexagonal phase (high chalcocite, temperatures between 380 and 708 K), and the high-temperature cubic phase above 708 K [38]. Earlier MDSs showed that the averaged Cu locations of Cu_2S in the hcp phase were at similar sites in the monoclinic phase [39]. The MDSs showed that trial-and-error refining of XRD data is insufficient to determine the crystal structures uniquely. Because the Cu ions increasingly acquire a liquidlike diffusing nature as the temperature increases, it is difficult to fit the structure; even partial-occupancy locations are used.

To remedy the situation, we utilized MDSs to investigate the diffusing nature of Cu atoms. Using first-principles RSSWO calculations, we obtained the five lowest energy structures from more than 100 initial guessed structures. The unit cells utilized for Cu_2S with hcp or fcc structures were set at an experimental lattice constant [40]. Sulfur atoms occupied the hexagonal sites of the hcp phase or the face-centered cubic sites of the fcc phase, forming the framework for Cu atoms' diffusion. For the hcp phase, the initial positions of Cu atoms were randomly generated using the RSSWO algorithm and distributed throughout the interstitial regions of the hexagonal S framework. For the fcc phase, we started by putting Cu atoms at $8c$ sites of $Fm\bar{3}m$ and then randomly displaced the Cu atoms to simulate their disorder nature. The optimal lowest energy structures were then obtained using DFT. For the MDSs, we used the NVT ensemble at temperatures of 450 K for the hcp phase and 750 K for the fcc phase, respectively. The MDSs for the hcp phase were performed using a $2\sqrt{3} \times 2\sqrt{3} \times 2$ unit cell (96 Cu and 48 S atoms) for 30 ps with a 1-fs time step, whereas the fcc phase was performed using a $2 \times 2 \times 2$ conventional unit cell (64 Cu and 32 S atoms) for 100 ps with 1-fs time step.

There are at least nine distinct partial-occupancy fits of Cu atoms reported in the literature for Cu_2S with cubic crystal symmetry, as illustrated in Fig. 5. A typical XRD structural analysis should be able to extract structural characteristics such as lattice parameters, crystal symmetry, atomic locations, and site occupancy from spectral descriptors. The XRD refinement approach has succeeded for material systems where the structures contain no mobile atoms. However, for liquidlike materials, such as Cu_2S or Cu_2Se , Cu ions are highly diffusive

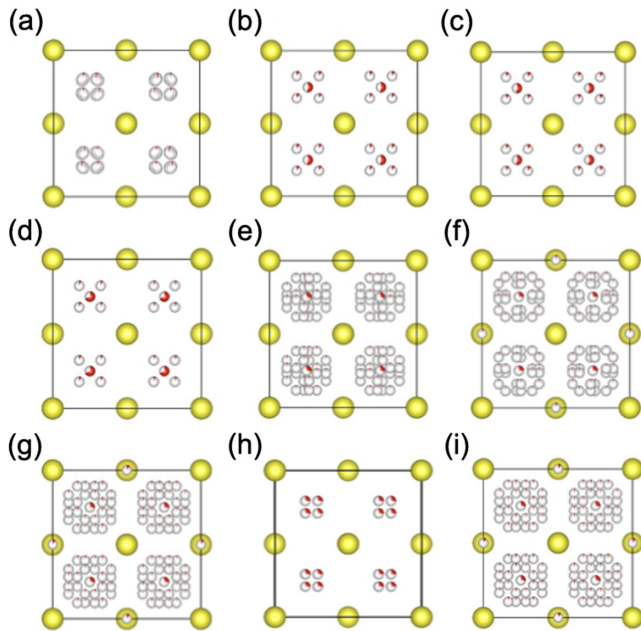


FIG. 5. (a)–(i) Crystal structures of Cu_2S reported in Refs. [40–45]. The red-white spheres represent the partially occupied Cu sites. Corresponding crystal structures were obtained from the Crystallography Open Database (COD) [23,24] (Table S3 of the Supplemental Material).

at higher temperatures (>400 K). Therefore, when conducting structural refinement, one frequently deals with a few tens of Bragg peaks. To this end, various partial occupancies may be achieved as a refined result to fit the XRD or ScXRD peak locations and intensities. Due to its trial-and-error nature, it is difficult to determine whether an XRD fitting result is correct and reliable, as evidenced by inconsistent results for Cu_2S shown in Fig. 5.

Figures 6(a) and 6(b) depict the 2D constant-density surfaces, with density equal to $3 \times 10^{-2} a_0^{-3}$, of the S and Cu 3D atomic density distributions for cubic Cu_2S at 750 K viewed along the [111] direction in a $2 \times 2 \times 2$ simulation cell. The density distributions of the S and Cu atoms exhibit extremely distinct behavior. The S atoms are entirely isolated to form spherical-shaped balls, while all Cu atoms are vibrating and diffusing to create tetragonal shapes to connect. The results indicate that the S atoms create the framework for the Cu atoms to diffuse and that both atom densities can be combined to generate the 3D-ADDF in a reduced $1 \times 1 \times 1$ unit cell. Figure 6(c) depicts the 2D constant-density surface map of Cu. Until now, calculated MDS results show no indication of crystal symmetry for the Cu_2S system. In fact, we find that three potential cubic space group symmetries, 202 ($Fm\bar{3}$), 209 ($F432$), 225 ($Fm\bar{3}m$), can be applied to the 3D-ADDF illustrated in Fig. 6(c) without affecting the structure and topology. Figures 6(d)–6(f) show the identical 2D constant-density surface map after applying space group symmetries $Fm\bar{3}$, $F432$, and $Fm\bar{3}m$, respectively. Indeed, there is no difference in the 2D maps even at the very low constant density of $3 \times 10^{-3} a_0^{-3}$; therefore any space group symmetry among the three symmetries may be designated as the crystal symmetry of Cu_2S . Since most experimental XRD findings

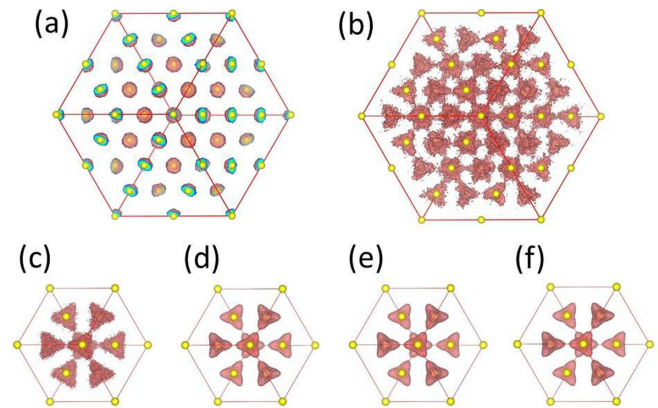


FIG. 6. (a) and (b) 2D constant-density surface, with density equal to $3 \times 10^{-2} a_0^{-3}$, of the S and Cu 3D atomic density distributions, respectively, for cubic Cu_2S at 750 K viewed along the [111] direction in a $2 \times 2 \times 2$ simulation cell. (c) The same Cu 2D constant-density surface map viewed in a reduced $1 \times 1 \times 1$ unit cell. (d)–(f) The same Cu 2D constant-density surface map after applying space group symmetries $Fm\bar{3}$, $F432$, and $Fm\bar{3}m$, respectively.

suggested that the symmetry for cubic Cu_2S is $Fm\bar{3}m$, we will examine the MDS results for cubic Cu_2S and Cu_2Se using the symmetry $Fm\bar{3}m$ in the following.

Figures 7(a)–7(f) show the 2D constant-density surface of the Cu 3D atomic density distribution function of the Cu_2S fcc phase at 750 K viewed along the [100], [110], and [111] directions at medium ($3 \times 10^{-2} a_0^{-3}$) and low ($6 \times 10^{-3} a_0^{-3}$) density values. There are two intriguing aspects worth mentioning here. First, as shown in Figs. 7(a)–7(c), although Cu atoms appear to be restricted to $8c$ sites, their vibration or diffusing behavior clearly shows a tetragonal symmetry nature. There is a lack of any other local maximum around the $8c$ sites [see Fig. 7(g)], and any partial occupancy of $192l$ of $Fm\bar{3}m$ detected by XRD could not represent the true structural factor. Second, by examining the Cu atom 2D constant-density surface in Figs. 7(d)–7(f), one can see that the distinct Cu high-density regions are connected through the entire unit cell at a lower density. Again, these linked distribution surfaces clearly define the Cu diffusing pathways and regions inside the crystal.

Figure 7(g) depicts a color-coded 2D atomic density map perpendicular to the $[1\bar{1}0]$ direction cut through the S atoms, with four tiny red spheres indicating the highest Cu density appearing at $8c$ sites. They are all single maxima, with the density decreasing monotonically away from the $8c$ sites; thus any partial occupancy with a $192l$ Wyckoff position is not appropriate or capable of describing the behavior of Cu atoms. Thus it is clear that the 3D-ADDF concept, rather than the partial-occupancy concept, should be used to study and understand the structural properties of Cu_2S . There are some small populated Cu densities at positions $(\frac{1}{4}, \frac{1}{4}, \frac{1}{2})$, $(\frac{3}{4}, \frac{3}{4}, \frac{1}{2})$, and $(\frac{1}{2}, \frac{1}{2}, \frac{1}{2})$, indicating the possibility of Cu ions sitting at the $48g$ site at $(\frac{1}{4}, \frac{1}{4}, \frac{1}{2})$ and at the $4b$ site at $(\frac{1}{2}, \frac{1}{2}, \frac{1}{2})$, which is consistent with the low occupation probability (4.75% at the $4b$ site) found from XRD refinement [40,46].

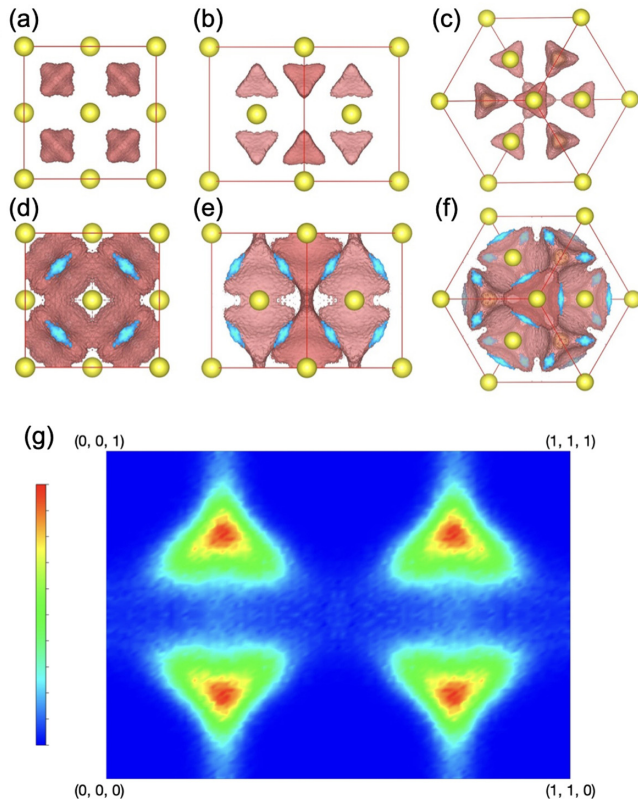


FIG. 7. (a)–(c) Cu 2D constant-density surface, with density equal to $3 \times 10^{-2} a_0^{-3}$, of the 3D atomic density distribution of cubic Cu_2S at 750 K viewed along the [100], [110], and [111] directions, respectively. (d)–(f) Same as (a)–(c), but for a Cu 2D constant-density surface with density equal to $6 \times 10^{-3} a_0^{-3}$. (g) Cu 2D atomic density distribution of cubic Cu_2S . The contour color plot parallels the (110) plane and passes through the cell center. The colors range from blue to red, corresponding to a density ranging from 0 to a maximum of $7.94 \times 10^{-2} a_0^{-3}$.

Another system that is similar to cubic Cu_2S is cubic Cu_2Se . The various XRD structural models of Cu_2Se suggested by experiment are summarized in Table S4 of the Supplemental Material [47–53]. Figures 8(a)–8(f) show the 2D constant-density surface of the Cu 3D atomic density distribution function of the cubic Cu_2Se phase at 600 K when viewed along the [100], [110], and [111] directions at medium ($3.5 \times 10^{-2} a_0^{-3}$) and low ($1 \times 10^{-2} a_0^{-3}$) density values. Figures 8(a)–8(c) depict the same Cu atom density confined at 8c sites with tetragonal symmetry [see Fig. 8(g)]. Although Figs. 8(d)–8(f) exhibit distinct 2D constant-density surfaces as compared with the Cu_2S case, the individual Cu high-density regions are nonetheless connected through the whole unit cell at a lower Cu density.

Figure 8(g) depicts a color-coded 2D atomic density plot perpendicular to the $[1\bar{1}0]$ direction that cuts through the S atoms, with four small red spheres indicating the highest Cu density appearing at 8c sites. In contrast to Cu_2S , which had two partial occupancies at the 48g and 4b sites, only one small populated Cu density appeared at the position $(\frac{1}{2}, \frac{1}{2}, \frac{1}{2})$, indicating a partial occupancy at the 4b site.

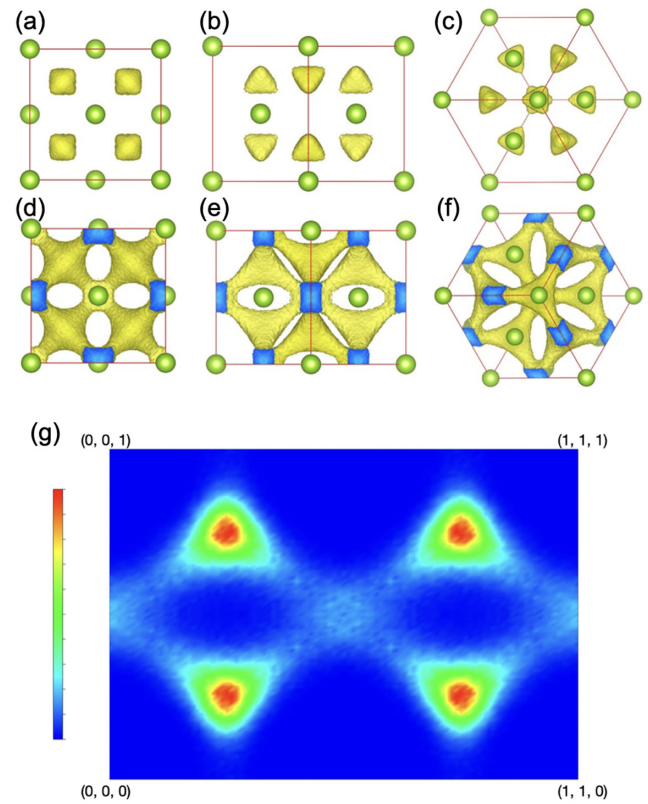


FIG. 8. (a)–(c) Cu 2D constant-density surface, with density equal to $3.5 \times 10^{-2} a_0^{-3}$, of the 3D atomic density distribution of cubic Cu_2Se at 600 K viewed along the [100], [110], and [111] directions, respectively. (d)–(f) Same as (a)–(c), but for a Cu 2D constant-density surface with density equal to $1 \times 10^{-2} a_0^{-3}$. (g) Cu 2D atomic density distribution of cubic Cu_2Se . The contour color plot parallels the (110) plane and passes through the cell center. The colors range from blue to red, corresponding to a density ranging from 0 to a maximum of $1.32 \times 10^{-1} a_0^{-3}$.

It is certainly interesting to examine the standard procedure for obtaining the 3D-ADDF from MDS results; here, we will utilize the Cu_2S hcp phase as an example to show the procedure. As we have used a $2\sqrt{3} \times 2\sqrt{3} \times 2$ unit cell for 30 ps with a 1-fs time step in five different MDS runs, we first accumulate the Cu atoms' positions into the primitive cell in each time frame and add up a total of 150 000 steps (or 30 000 time steps per MD run \times 5 MD runs) to obtain the Cu atomic density distribution function, represented by density values at $100 \times 100 \times 100$ grid points inside the unit cell, with normalization of four Cu atoms inside the primitive hcp unit cell. Figures 9(a) and 9(b) depict the 2D constant-density surface of the Cu 3D atomic density distribution function of the Cu_2S hcp phase at 450 K viewed along the [001] and [110] directions at medium density ($2 \times 10^{-2} a_0^{-3}$) before any symmetry operation. As can be seen in Fig. 9(a), there is a threefold rotation symmetry, and Fig. 9(b) shows an inversion symmetry and a mirror plane symmetry passing through the S atom perpendicular to the z direction, indicating that the best symmetry operation for this phase is obviously $P\bar{3}1c$ (space group 163). It is worth noting that this is a different symmetry from the one typically suggested by experiment, which is $P6_3/mmc$ (space group 194). Figures 9(c) and 9(d)

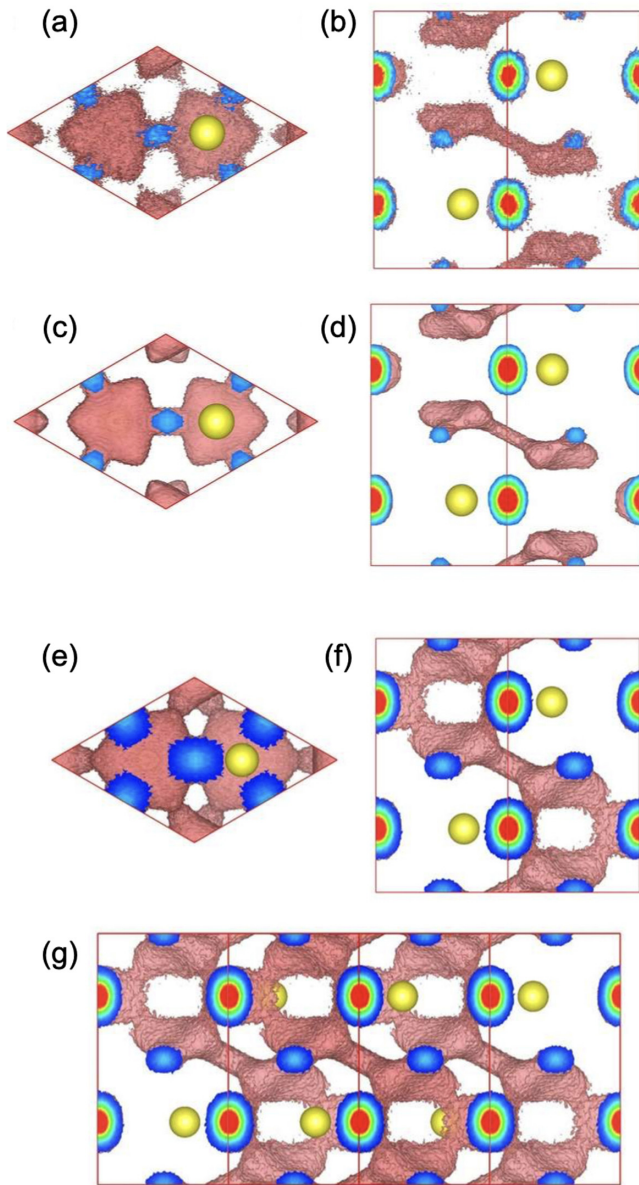


FIG. 9. (a)–(d) 2D constant-density surface, with density equal to $2 \times 10^{-2} a_0^{-3}$, of the Cu 3D atomic density distribution of hcp Cu_2S at 450 K viewed along the [001] and [110] directions before [(a) and (b)] and after [(c) and (d)] applying the symmetry operation. (e)–(g) 2D constant-density surface, with density equal to $5 \times 10^{-3} a_0^{-3}$, of the Cu 3D atomic density distribution of hcp Cu_2S at 450 K viewed along the [001] and [110] directions. (g) 2D constant-density surface with a $2 \times 2 \times 1$ unit cell showing the Cu atoms’ diffusion paths.

show the 2D constant-density surface of the Cu 3D atomic density distribution after the $P\bar{3}1c$ symmetry operation. As one can see, the Cu density does not change its topology, indicating that the $P\bar{3}1c$ symmetry is indeed the correct symmetry for the system. Figures 9(e)–9(g) depict the 2D constant-density surface at lower ($5 \times 10^{-3} a_0^{-3}$) values; once again, this constant-density surface defines the diffusing pathways for Cu atoms, as shown in Fig. 9(g), within a $2 \times 2 \times 1$ unit cell.

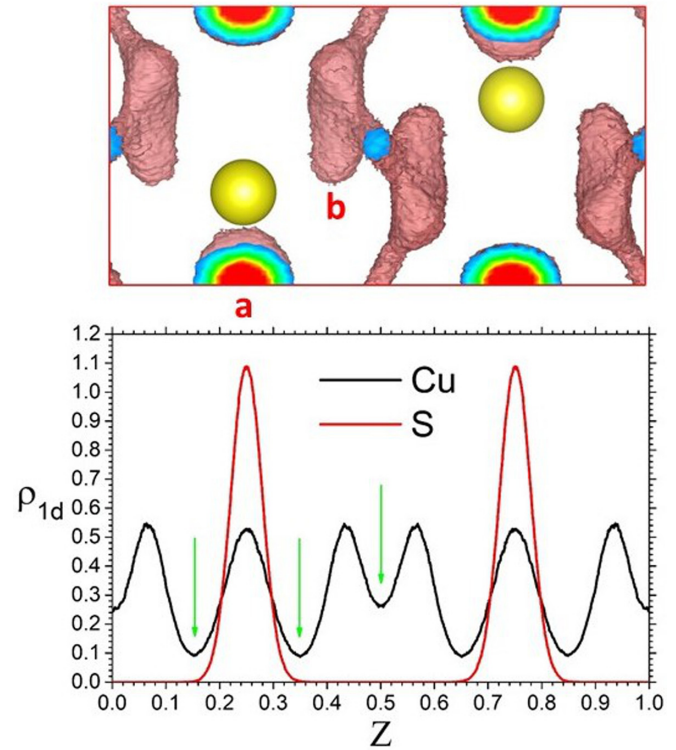


FIG. 10. The 1D atom density along the z direction of hcp Cu_2S at 450 K.

Finally, because the 3D-ADDF is the accumulated atom density, if there is a maximum density corresponding to an atom, one can integrate all the densities near the maximum point to obtain the total amount of partial occupancy. Here, we use hcp Cu_2S as an example to illustrate this point. The one-dimensional atomic density of hcp Cu_2S at 450 K along the [001] direction and its corresponding constant-density surface of the 3D-ADDF viewed along the [110] direction are shown in Fig. 10. For the S density, there are two peaks corresponding to S atoms at $(\frac{1}{3}, \frac{1}{3}, \frac{1}{4})$ and $(\frac{2}{3}, \frac{2}{3}, \frac{3}{4})$; however, for Cu atoms, there are six peaks divided into two groups: (i) z at 0.25 and 0.75 with a round ball shape and (ii) z at 0.075, 0.425, 0.575, and 0.925 with a flat equilateral triangle shape with three maxima [refer to Fig. 9(a)]. The round ball shape of the Cu density, denoted by the red “a” ($0.15 < z < 0.35$), has a total integrated amount of Cu partial occupancy of 0.734, while the flat equilateral triangle shape, denoted by the red “b” ($0.35 < z < 0.50$), has a total integrated amount of Cu partial occupancy of 0.633. This result is consistent with the previous $\beta\text{-Cu}_2\text{S}$ MD findings that about 38% of Cu atoms are in the intralayer and 62% of Cu atoms are in the interlayer region between two S layers [15]. The example Cu_2S hcp phase demonstrated here has proved that the partial occupancy can be obtained automatically by integrating the atom density near the density maximum without the need for the trial-and-error process used in XRD. This procedure is a significant step and improvement in the theoretical approach for studying materials systems with mobile atoms inside the crystal.

IV. CONCLUSION

To summarize, for materials systems with part of their atoms diffusing or hopping inside the crystal below the melting temperature, fitting or determining the structure becomes difficult or impossible, even assisted with the partial-occupancy concept. This fact is because finite partial-occupancy positions are insufficient and unsuitable for describing the behavior of diffusing or hopping atoms. To address this issue, we propose running molecular dynamics simulations to generate a three-dimensional atomic density distribution function by adding all the atoms in each time step and putting all the atoms of the supercell into the reduced $1 \times 1 \times 1$ or primitive unit cell. The obtained 3D-ADDF will

automatically reveal or hint at the existing symmetry presented in the system. The final results of the 3D-ADDF will provide the most fundamental structural properties, including (i) the diffusing paths and regions of highly mobile atoms, (ii) the quantitative partial occupancy and positions of each type of atom inside the unit cell, and (iii) the appropriate and correct system symmetry.

ACKNOWLEDGMENTS

This work is supported by the Ministry of Science and Technology of Taiwan under Grant No. MOST 108-2112-M-001-043-MY3 and the Center for Sustainability Science, Academia Sinica, under Project No. AS-SS-109-01-4.

-
- [1] H. Liu, X. Shi, F. Xu, L. Zhang, W. Zhang, L. Chen, Q. Li, C. Uher, T. Day, and G. J. Snyder, Copper ion liquid-like thermoelectrics, *Nat. Mater.* **11**, 422 (2012).
- [2] K. Zhao, P. Qiu, X. Shi, and L. Chen, Recent advances in liquid-like thermoelectric materials, *Adv. Funct. Mater.* **30**, 1903867 (2020).
- [3] Z. Zhang, K. Zhao, T.-R. Wei, P. Qiu, L. Chen, and X. Shi, Cu₂Se-based liquid-like thermoelectric materials: looking back and stepping forward, *Energy Environ. Sci.* **13**, 3307 (2020).
- [4] P. C. Wei, C. N. Liao, H. J. Wu, D. Yang, J. He, G. V. Biesold-McGee, S. Liang, W. T. Yen, X. Tang, W. J. Yeh, Z. Lin, and J. H. He, Thermodynamic routes to ultralow thermal conductivity and high thermoelectric performance, *Adv. Mater. (Weinheim)* **32**, 1906457 (2020).
- [5] W.-D. Liu, L. Yang, Z.-G. Chen, and J. Zou, Promising and eco-friendly Cu₂X-based thermoelectric materials: Progress and applications, *Adv. Mater. (Weinheim)* **32**, 1905703 (2020).
- [6] P. Lukashev, W. R. L. Lambrecht, T. Kotani, and M. van Schilfgaarde, Electronic and crystal structure of Cu_{2-x}S: Full-potential electronic structure calculations, *Phys. Rev. B* **76**, 195202 (2007).
- [7] P. Vaqueiro, G. Guelou, A. Kaltzoglou, R. I. Smith, T. Barbier, E. Guilmeau, and A. V. Powell, The influence of mobile copper ions on the glass-like thermal conductivity of copper-rich tetrahedrites, *Chem. Mater.* **29**, 4080 (2017).
- [8] B. Jiang, P. Qiu, E. Eikeland, H. Chen, Q. Song, D. Ren, T. Zhang, J. Yang, B. B. Iversen, X. Shi, and L. Chen, Cu₈GeSe₆-based thermoelectric materials with an argyrodite structure, *J. Mater. Chem. C* **5**, 943 (2017).
- [9] S. Lin, W. Li, and Y. Pei, Thermally insulative thermoelectric argyrodites, *Mater. Today* **48**, 198 (2021).
- [10] X. He, Y. Zhu, A. Epstein, and Y. Mo, Statistical variances of diffusional properties from *ab initio* molecular dynamics simulations, *npj Comput. Mater.* **4**, 18 (2018).
- [11] L. Xie, D. Wu, H. Yang, Y. Yu, Y. Wang, and J. He, Direct atomic-scale observation of the Ag⁺ diffusion structure in the quasi-2D liquid-like state of superionic thermoelectric AgCrSe₂, *J. Mater. Chem. C* **7**, 9263 (2019).
- [12] N. J. J. de Klerk, I. Rosłóń, and M. Wagemaker, Diffusion mechanism of Li argyrodite solid electrolytes for Li-ion batteries and prediction of optimized halogen doping: The effect of Li vacancies, halogens, and halogen disorder, *Chem. Mater.* **28**, 7955 (2016).
- [13] H. Kim, S. Ballikaya, H. Chi, J.-P. Ahn, K. Ahn, C. Uher, and M. Kaviani, Ultralow thermal conductivity of β -Cu₂Se by atomic fluidity and structure distortion, *Acta Mater.* **86**, 247 (2015).
- [14] K. Zhuo, J. Wang, J. Gao, U. Landman, and M.-Y. Chou, Liquidlike Cu atom diffusion in weakly ionic compounds Cu₂S and Cu₂Se, *Phys. Rev. B* **102**, 064201 (2020).
- [15] J. Wang, K. Zhuo, J. Gao, U. Landman, and M.-Y. Chou, Mechanism for anisotropic diffusion of liquid-like Cu atoms in hexagonal β -Cu₂S, *Phys. Rev. Materials* **5**, 073603 (2021).
- [16] A. J. E. Rettie, J. Ding, X. Zhou, M. J. Johnson, C. D. Malliakas, N. C. Osti, D. Y. Chung, R. Osborn, O. Delaire, S. Rosenkranz, and M. G. Kanatzidis, A two-dimensional type I superionic conductor, *Nat. Mater.* **20**, 1683 (2021).
- [17] S. Kumar, M. K. Gupta, P. Goel, R. Mittal, O. Delaire, A. Thamizhavel, S. Rols, and S. L. Chaplot, Solidlike to liquid-like behavior of Cu diffusion in superionic Cu₂X (X = S, Se): An inelastic neutron scattering and *ab initio* molecular dynamics investigation, *Phys. Rev. Materials* **6**, 055403 (2022).
- [18] D. C. Wych, J. S. Fraser, D. L. Mobley, and M. E. Wall, Liquid-like and rigid-body motions in molecular-dynamics simulations of a crystalline protein, *Struct. Dyn.* **6**, 064704 (2019).
- [19] S. W. Wang, C. R. Hsing, and C. M. Wei, Expedite random structure searching using objects from Wyckoff positions, *J. Chem. Phys.* **148**, 054101 (2018).
- [20] F. Boucher, M. Evain, and R. Brec, Distribution and ionic diffusion path of silver in γ -Ag₈GeTe₆: A temperature dependent anharmonic single crystal structure study, *J. Solid State Chem.* **107**, 332 (1993).
- [21] S. Geller, The crystal structure of γ Ag₈GeTe₆, a potential mixed electronic-ionic conductor, *Z. Kristallogr. - Cryst. Mater.* **149**, 31 (1979).
- [22] N. Rysanek, P. Laruelle, and A. Katty, Structure cristalline de Ag₈GeTe₆ (γ), *Acta Crystallogr., Sect. B: Struct. Sci.* **32**, 692 (1976).
- [23] R. T. Downs and M. Hall-Wallace, The American Mineralogist Crystal Structure Database, *Am. Mineral.* **88**, 247 (2003).
- [24] A. Vaitkus, A. Merkys, and S. Gražulis, Validation of the Crystallography Open Database using the Crystallographic Information Framework, *J. Appl. Crystallogr.* **54**, 661 (2021).

- [25] P. Hohenberg and W. Kohn, Inhomogeneous electron gas, *Phys. Rev.* **136**, B864 (1964).
- [26] W. Kohn and L. J. Sham, Self-consistent equations including exchange and correlation effects, *Phys. Rev.* **140**, A1133 (1965).
- [27] G. Kresse and J. Hafner, *Ab initio* molecular dynamics for open-shell transition metals, *Phys. Rev. B* **48**, 13115 (1993).
- [28] G. Kresse and J. Furthmüller, Efficiency of ab-initio total energy calculations for metals and semiconductors using a plane-wave basis set, *Comput. Mater. Sci.* **6**, 15 (1996).
- [29] P. E. Blöchl, Projector augmented-wave method, *Phys. Rev. B* **50**, 17953 (1994).
- [30] J. P. Perdew, K. Burke, and M. Ernzerhof, Generalized Gradient Approximation Made Simple, *Phys. Rev. Lett.* **77**, 3865 (1996).
- [31] K. Momma and F. Izumi, *VESTA 3* for three-dimensional visualization of crystal, volumetric and morphology data, *J. Appl. Crystallogr.* **44**, 1272 (2011).
- [32] F. Boucher, M. Evain, and R. Brec, Single-crystal structure determination of γ -Ag₈SiTe₆ and powder X-ray study of low-temperature α and β phases, *J. Solid State Chem.* **100**, 341 (1992).
- [33] See Supplemental Material at <http://link.aps.org/supplemental/10.1103/PhysRevMaterials.6.083601> for details of the lowest-energy initial structures, MD trajectories of Ag₈SiTe₆, and mean-square displacements, pair correlation functions, and also experimental suggested structural models of Ag-based argyrodites and Cu₂X-based materials.
- [34] G. Trimarchi, Z. Wang, and A. Zunger, Polymorphous band structure model of gapping in the antiferromagnetic and paramagnetic phases of the Mott insulators MnO, FeO, CoO, and NiO, *Phys. Rev. B* **97**, 035107 (2018).
- [35] X. G. Zhao, G. M. Dalpian, Z. Wang, and A. Zunger, Polymorphous nature of cubic halide perovskites, *Phys. Rev. B* **101**, 155137 (2020).
- [36] Z. Wang, X. G. Zhao, R. Koch, S. J. L. Billinge, and A. Zunger, Understanding electronic peculiarities in tetragonal FeSe as local structural symmetry breaking, *Phys. Rev. B* **102**, 235121 (2020).
- [37] X. G. Zhao, Z. Wang, O. I. Malyi, and A. Zunger, Effect of static local distortions vs. dynamic motions on the stability and band gaps of cubic oxide and halide perovskites, *Mater. Today* **49**, 107 (2021).
- [38] D. J. Chakrabarti and D. E. Laughlin, The Cu-S (copper-sulfur) system, *Bull. Alloy Phase Diagrams* **4**, 254 (1983).
- [39] L. W. Wang, High Chalcocite Cu₂S: A Solid-Liquid Hybrid Phase, *Phys. Rev. Lett.* **108**, 085703 (2012).
- [40] G. Will, E. Hinze, and A. R. M. Abdelrahman, Crystal structure analysis and refinement of digenite, Cu_{1.8}S, in the temperature range 20 to 500 °C under controlled sulfur partial pressure, *Eur. J. Mineral.* **14**, 591 (2002).
- [41] M. J. Buerger and B. J. Wuensch, Distribution of atoms in high chalcocite, Cu₂S, *Science* **141**, 276 (1963).
- [42] N. Morimoto and G. Kullerud, Polymorphism in digenite, *Am. Mineral.* **48**, 110 (1963).
- [43] R. J. Cava, R. K. McMullan, and B. J. Wuensch, Mobile ion distribution and anharmonic thermal motion in fast ion conducting Cu₂S, *Solid State Ionics* **5**, 501 (1981).
- [44] M. Oliveria, R. K. McMullan, and B. J. Wuensch, Single crystal neutron diffraction analysis of the cation distribution in the high-temperature phases α -Cu_{2-x}S, α -Cu_{2-x}Se, and α -Ag₂Se, *Solid State Ionics* **28–30**, 1332 (1988).
- [45] K. Yamamoto and S. Kashida, X-ray study of the average structure of Cu₂Se and Cu_{1.8}S in the room temperature and high temperature phases, *J. Solid State Chem.* **93**, 202 (1991).
- [46] B. J. Wuensch and M. J. Buerger, Crystal structure of chalcocite, Cu₂S, *Miner. Soc. Am. Spec.* **1**, 164 (1963).
- [47] K. D. Machado, J. C. de Lima, T. A. Grandi, C. E. M. Campos, C. E. Maurmann, A. A. M. Gasperini, S. M. Souzaa, and A. F. Pimentab, Structural study of Cu_{2-x}Se alloys produced by mechanical alloying, *Acta Crystallogr., Sect. B: Struct. Sci.* **60**, 282 (2004).
- [48] W. Borchert, Gitterumwandlungen im System Cu_{2-x}Se, *Z. Kristallogr. - Cryst. Mater.* **106**, 5 (1945).
- [49] S. A. Danilkin, A. N. Skomorokhov, V. Rajevac, A. Hoser, H. Fuess, and N. N. Bickulova, Crystal structure and lattice dynamics of superionic copper selenide Cu_{2-d}Se, *J. Alloys Compd.* **361**, 57 (2003).
- [50] E. Eikeland, A. B. Blichfeld, K. A. Borup, K. P. Zhao, J. Overgaard, X. Shi, L. D. Chen, and B. B. Iversen, Crystal structure across the β to α phase transition in thermoelectric Cu_{2-x}Se, *IUCrJ* **4**, 476 (2017).
- [51] R. D. Heyding and R. M. K. Murray, Crystal structures of Cu_{1.8}Se, Cu₃Se₂, α - and γ -CuSe, CuSe₂, and CuSe₂ II, *Can. J. Chem.* **54**, 841 (1976).
- [52] P. Rahlfs, Über die kubischen Hochtemperaturmodifikationen der Sulfide und Telluride des Silbers und des einwertigen Kupfers, *Z. Phys. Chem., Abt. B* **31B**, 157 (1936).
- [53] T. Sakuma, K. Sugiyama, E. Matsubara, and Y. Waseda, Determination of the crystal structure of superionic phase of Cu₂Se, *Mater. Trans., JIM* **30**, 365 (1989).